

Investigating the Properties of Asteroids, focusing on 694 Ekard.

Sharif Khan-Bennett

Co-Investigators:

Maciej Dabrowny

Ciaran Garden

Astle Fernandez



School of Physics and Astronomy
University of Birmingham
United Kingdom
January 24, 2020

Abstract

This investigation aims to determine key properties of asteroids to assess their suitability for asteroid mining. The indicators used to judge this include rotational period, geometric albedo, mass, and volume. Three asteroids were selected for observation; these were 18172 (2000 QL7), 162723 (2000 VM) and 99248 (2001 KY66). Unfortunately, unfavourable weather conditions throughout November 2019 meant that we were unable to observe these targets, instead, archival data available thanks to Sean McGee and the JPL Horizons database were used. Despite being unable to observe these targets, the criteria for asteroid selection as well as the reduction procedure was still applicable for the archival data, hence being described in section 2.1. 694 Ekard was chosen as a backup target and its rotational period, geometric albedo and diameter were found to be $5.87^{+2.71}_{-1.02}h$, one standard deviation away from online predictions, 0.025 ± 0.001 , one standard deviation from online predictions, and 121.891 ± 3.657 km agreeing with predictions to 3d.p respectively.

Contents

| | | |
|----------|---|-----------|
| 1 | Introduction | 2 |
| 2 | Theory and Procedure | 3 |
| 2.1 | Observation | 3 |
| 2.1.1 | Constraining Coordinates | 3 |
| 2.1.2 | Data Processing | 5 |
| 2.1.3 | Object Extraction | 6 |
| 2.2 | Finding rotational period | 6 |
| 2.3 | Finding geometric albedo | 8 |
| 2.3.1 | The "1329 Relation" | 8 |
| 2.3.2 | Phase Model | 9 |
| 3 | Results and analysis | 11 |
| 3.1 | Rotational period | 11 |
| 3.2 | Shape and Geometric albedo | 12 |
| 3.2.1 | Determining the Shape | 12 |
| 3.2.2 | Geometric Albedo | 13 |
| 4 | Conclusion and Further Areas of Research | 15 |
| 5 | Acknowledgements | 16 |
| 6 | Appendix | 17 |

1 Introduction

Asteroids are remnants of the very early solar system which have been preserved due to the low probability of them colliding with other objects, they are often rich with metals and minerals. During the formation of the Earth, heavier metals including Iron and Nickel sunk to its core, leaving the crust depleted of these elements. This deficiency was replenished by the accumulation of metal found in asteroids during showers such as the late-heavy bombardment 4 billion years ago [1]. Therefore, in addition to being extremely valuable sources of information about the early solar system, asteroids have a direct monetary value due to the metal ores they hold. It is predicted that there are still many thousands of metal-rich asteroids in the main asteroid belt [1]. With this abundance in mind, the skies are appearing as ever more appealing sites to mine for rare metals including Gold, Platinum, Iron and Nickel. This may be the future of metal ore mining, especially when considering the limited resources left on Earth; predictions suggest that within the next 20 years, the rate of production of Iron will decrease as a result of ore depletion [2].

This investigation aims to characterise 694 Ekard and determine whether it is a suitable candidate for asteroid mining. Properties of an ideal candidate include a small rotational period, large albedo and large mass. A small period is necessary so that ore extraction would be feasible without needing to enter a “geostationary orbit” around the asteroid to land, see appendix 1. A larger mass is ideal because it could suggest a greater quantity of metal present, increasing the likelihood of a mission being economically feasible. An asteroid with a large albedo is ideal because, like having a larger mass, it could indicate a greater proportion of metal. The albedo is a ratio of the incident flux to the reflected flux. A larger albedo indicates a shinier surface, possibly due to the presence of more metal. Its composition will be estimated by determining its taxonomic class. The main asteroid classes include C-type, carbonaceous asteroids, mostly composed of clay and rock, M-type, metallic asteroids which contain nickel and iron and S-type, siliceous asteroids which contain metal silicates[3]. As well as suggesting its composition, each class has a range of expected values for albedo and density. Hence, the albedo will be used to estimate these properties. This method is somewhat crude and assumes that the proportions of metal on the surface are representative of its bulk composition. More accurate methods are discussed in the conclusion.

To determine the rotational period, the object’s lightcurve will be extracted from observational data taken in November 2019. A lightcurve is a plot of received flux against time where variations in it are expected from the following two effects. One is the result of changes in the object-observer and the object-solar distances and another as a result of the rotation of the asteroid. Variations from changing distances can be understood from the inverse-square law and are removed via normalisation. They are removed because we aim to discover the intrinsic properties of the asteroid as opposed to its orbital parameters. The rotation affects the received flux through two contributing effects. Firstly, as the asteroid rotates, its projected area, tangential to our line of sight changes due to its irregular shape, altering the amount of light that it can reflect in our direction. Secondly, a non-uniform surface composition will also result in fluctuations in the lightcurve due to some materials on the surface of the asteroid being more reflective than others. Rotational effects of an asteroid manifest in a lightcurve via three composite sine waves; a result of the asteroid rotating independently about three perpendicular axes. This lightcurve can be analysed with sine wave fitting and by Fourier analysis to find the rotational period.

When calculating the albedo, the JPL Horizons database available through the asteroquery module was used as the source of data. The reason is that it provided an angular width and object-observer distance measurements, allowing for the calculation of the projected area as a

function of time. This is crucial in finding an accurate measurement of albedo since it is highly dependent on the reflecting area. Initially, the “1329 relation” [4], which relates the albedo to the diameter and absolute magnitude will be applied to find the albedo so that this result can be used as a standard of comparison. Then, the albedo will be found by using the model, as suggested by Bowell et al. 1989 [5] whereby finding the irradiance factor at opposition (phase angle of zero) via extrapolation. Both these methods are explained in detail in section 2.3.

2 Theory and Procedure

2.1 Observation

2.1.1 Constraining Coordinates

Selecting a suitable asteroid for observation requires the application of constraints on the Right Ascension (RA) and Declination (DEC), dependant on the location of the observer on Earth. This limits the asteroids to the ones which are above the horizon during observations. In order to reduce airmass, the minimum elevation (ϕ) was set 40° above the horizon. This gives a maximum airmass of 1.56. Along with the latitude of the West Hills Observatory(θ) the declination of objects (δ) can be constrained as demonstrated by figure 1, and calculated in equation 1.

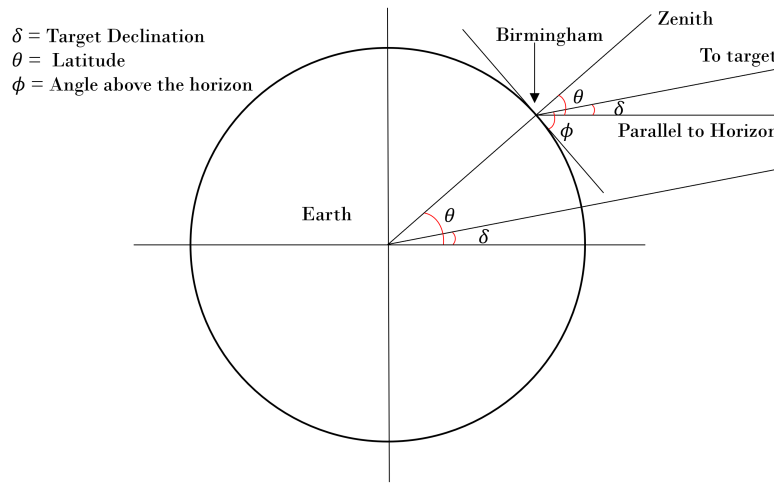


Figure 1: Schematic of the geometry of observations made from Birmingham, where $\theta \simeq 52^\circ$, and $\phi = 40^\circ$.

$$\delta = \theta \pm 90 \mp \phi \quad (1)$$

The \pm signs are present in equation 1 so that objects on either side of the zenith are considered. By setting theta to the latitude of Birmingham, 52° , DEC limits are obtained to be between 2° and 102° .

To determine the constraints on RA of potential objects, the RA of the sun on the date of observation must be considered. This is found using knowledge that the Sun has an RA of

zero at the spring equinox. Since observations are planned to be made in November, 8 months later, the Sun's RA can be found to be $24/12 \times 8 = 16h$ in November. Therefore, objects that cross the meridian at midnight have RA's 12 hours later, equal to 4h by applying a 24-hour periodicity. Observations are intended to take place between 18:00 and 22:00, translating to RA limits between 22h and 2h.

As well as constraining coordinates such that only objects above Birmingham in November are selected, constraints on apparent magnitude must also be applied to ensure that a compelling signal to noise ratio, SNR, is attained (at least equal to 5). To get an upper observing limit for magnitude, regardless of condition, bright conditions were assumed in accord with the point source and surface brightness sensitivity limits of the SBIG STX-16803 camera at the West Hills Observatory. For an SNR of 5 and exposure time of 10 minutes, a maximum magnitude of 16.7 is possible for candidates[6].

Additionally, ensuring there was a suitable asteroid for observation throughout November was essential to be flexible in response to unpredictable weather. Therefore, three asteroid candidates were selected, each peaking in the night sky at different points in November. Figure 2 summarises these asteroids which peak in early, mid and late November respectively. Despite 99248 (2001 KY66) falling outside of the determined limits on RA, its very large DEC meant that it was still observable in the night sky. As we intended to capture a full period for the asteroids, 8 hours of observing time were requested. Since no previous attempts to measure the period for these asteroids had been made, an estimation of this was used, relying on the suggestion that 8-12 hours was a typical rotational period for asteroids[7].

| Target name | RA (J2000) | Dec (J2000) | Filter | Time (hrs) | Comment |
|-------------------|---------------|----------------|--------|---------------|--|
| 18172 (2000 QL7) | 00:25:00 | +74:54:00 | V | 8 | Coords Taken: 10th Nov (Bright) Observable: Oct-19th Nov |
| 162723 (2000 VM) | 01:03:00 | +47:42:00 | V | 8 | Coords Taken: 18th Nov (Grey) Observable: 5th-23rd Nov |
| 99248 (2001 KY66) | 05:15:00 | +50:00:00 | V | 8 | Coords Taken 24th Nov Observable: 10th-30th Nov (Dark) |

Figure 2: Summary of proposed targets including coordinates, observation filters, observing time and dates of when each asteroid was highest in the sky.

The dimmest of our targets were predicted to have a magnitude of 16.5 this allowed for the integration time (time over which observation frames are stacked) to be calculated. An SNR of 10 was selected to improve accuracy. As before, bright conditions were assumed to get an upper limit of integration time, and the choice of the dimmest target for calculation ensured that at least this SNR value would be reached for all of the targets per frame. Using these values, an integration time of 28.9 minutes was obtained, see appendix 2 for calculation. This was to be done over 6 5-minute exposures to avoid the image blurring as a result of the movement of the asteroid during the exposure, as well as to minimise the chance of pixel saturation. Observations would be repeated over 8 hours to sample the asteroid's full period.

2.1.2 Data Processing

To calibrate the data, dark, flat and bias frames were also to be taken on the night of observation. Typically, the dark frames would have a negligible effect due to the efficient cooling of the CCD, however, to include all sources of error, they were taken into account during the reduction process. Dark frames would be recorded by taking observations with the shutter closed for the same amount of time as (or scaled to match) the science frames such that the only signal is as a result of thermally-excited electrons. Flat frames need to be taken into account to include errors as a result of the non-uniform sensitivity of the pixels in the CCD. This can be measured by pointing the telescope at a uniform source of light, such as the sky during twilight and measuring the variation. Bias is an additional source of random error as a result of readout noise. The pixel count follows a Gaussian distribution, therefore, some pixels may be measured to have a negative count of electrons which makes no physical sense. To solve this, an offset voltage is applied. The bias level is then measured by taking frames with zero exposure time, to subtract from the science frames.

Once all the frames were collected, the data reduction process was applied using IRAF. All the bias frames were combined into a master bias and subtracted from each dark and flat frame. The resultant dark frames were combined into a master dark and re-scaled to ensure a matching exposure time to the science frame. This was then subtracted from the bias-subtracted flat frames. Each of the new flat frames was normalised to ensure a pixel count of unity and then combined to a master flat. The master bias and master dark were subtracted from each science frame which was then divided by the master flat, giving the processed science frames. Finally, all the science frames were aligned such that the background stars remained stationary and the target was the only object that moved between frames.

As alluded to in the abstract, poor weather meant we were unable to do this with the asteroids in figure 2, and so had to rely on archival data. By applying the same selection process, 694 Ekard was chosen as our asteroid for investigation as it had an RA of 1^h32^m and a DEC of $20^\circ 23'$, complying with the constraints defined in section 2.1.1. It is also quoted to have a relatively short rotational period of $5.925h$ [8] meaning an entire period could be observed. Figure 3 shows its staralt diagrams on the month of observation. The data archive included 460 bias, dark, flat and science frames which underwent the same reduction process outlined for our initial targets.

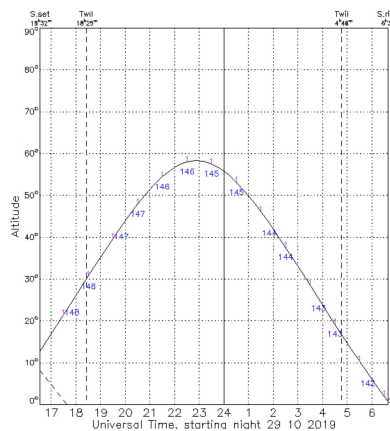


Figure 3: Staralt diagram for 694 Ekard on the 29/10/19. It can be seen that it peaks at around 23:00, at which point observations incur an airmass of $\simeq 1.15$ [9].

2.1.3 Object Extraction

An initial attempt of object extraction was made whereby a mean count of each pixel was taken across all the frames to be subtracted from each frame. The desired effect would be that all the pixels with constant magnitudes during the observation would be removed. When put into practice, this technique took too long. This was because no pixels received a constant flux during the observation due to changing seeing effects. Consequently, a different approach was applied; DS9 was used to find the initial and final x-pixel and y-pixel coordinates from the observation. A box was then drawn enclosing this line from corner to corner so that anything on the outside of the box could be disregarded. Next, a python code was written to plot the coordinates of 694 Ekard across the science frames. The results are seen in figure 4, where the red line is the trajectory of the asteroid.

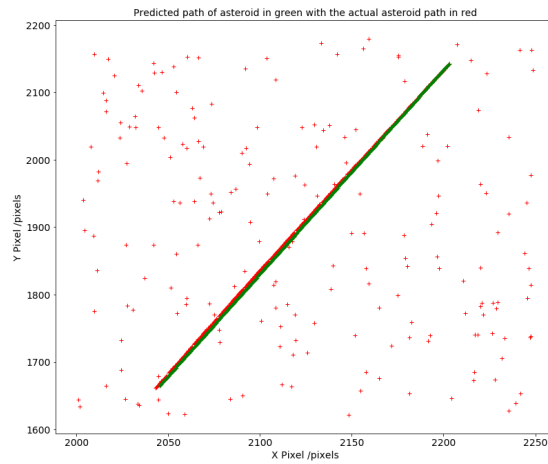


Figure 4: The trajectory of 694 Ekard during the observation. The red line indicates the actual path taken, while the green line is the straight-line model plotted by considering the total change in x and y coordinate. The other red crosses are background stars in the frame.

The gradient of this line was found by dividing the change in x and y coordinates by the number of frames. This line was applied to the minimum x and y coordinates to plot a straight line, as seen by the green line in figure 4. In order to extract the asteroid from the data, points which lie more than 5σ away from the straight-line plot were discounted. The magnitude of each point was found using SExtractor. This was done by setting the SATUR_LEVEL to 510000ADU , the PIXEL_SCALE to $0.467\text{arcsecond mm}^{-1}$ and the GAIN to $1.27e^{-}\text{ADU}^{-1}$. The zero point magnitude was found to be 23.8312 ± 0.0007 by measuring the magnitude of a known source in the frame.

2.2 Finding rotational period

Two methods were applied to find the rotational period, the first involves fitting sine waves to the data and recording their frequencies. The second involves using a Fourier transform to find the frequencies of each component of rotation.

The magnitude was plotted against time, as seen in figure 5. It can be seen from the graph

that there is a lot of random error as a result of seeing effects in the atmosphere, such as clouds or turbulent air. In order to remove these unwanted effects, the magnitude variation of six constant stars in the frame were considered: any variation on these stars would have been dominated by seeing effects. The magnitudes of the six stars were averaged across the frames and then subtracted from each frame to show the variation from seeing effects as a function of time, as seen in figure 5b. Removing this variation from the magnitude of points deemed to be the asteroid, and plotting against time gives figure 5c.

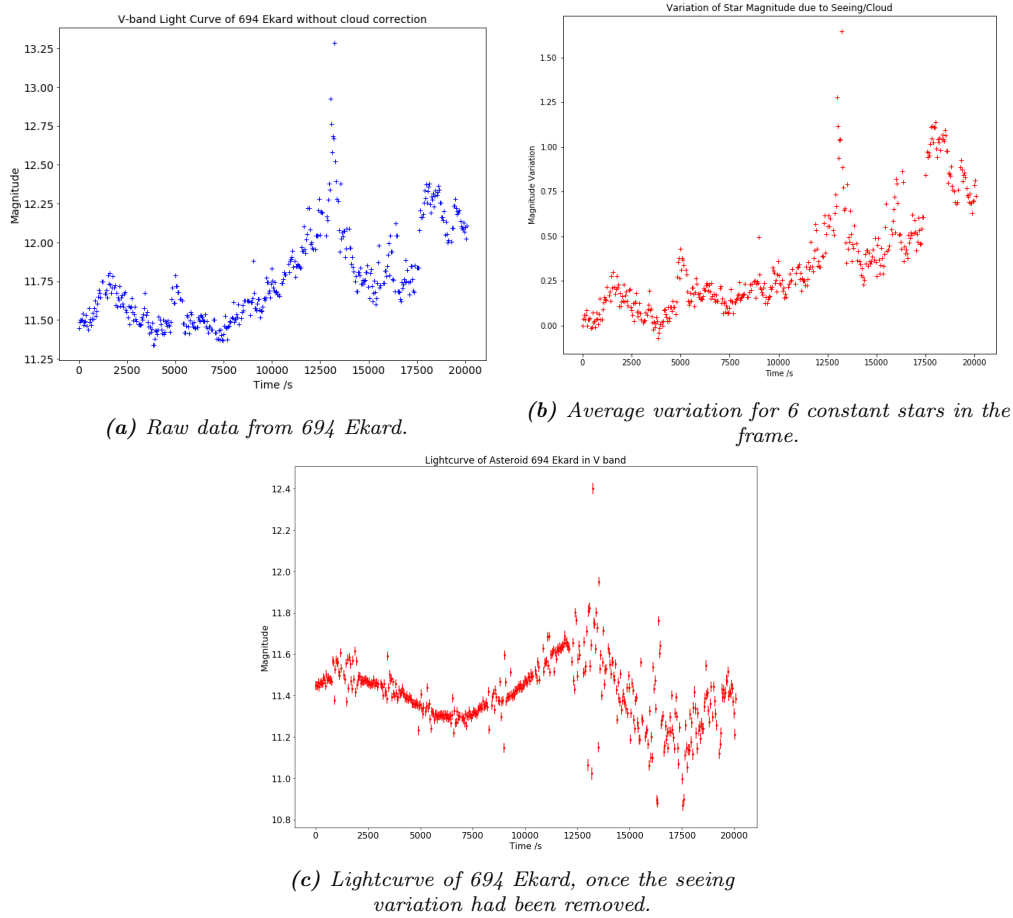
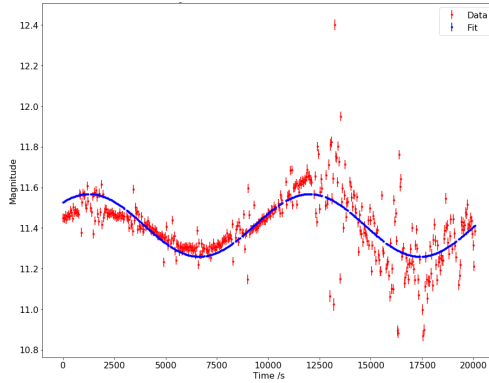


Figure 5: Three plots of magnitude against time. The similarity between (a) and (b) indicates that the main contributing effect to the apparent magnitude was from seeing effects. Removing these from the raw data for 694 Ekard obtains its lightcurve, as seen in (c). It can be seen that the quality of the data diminishes over the course of the observation, this is presumed to be as a result of worsening weather conditions.

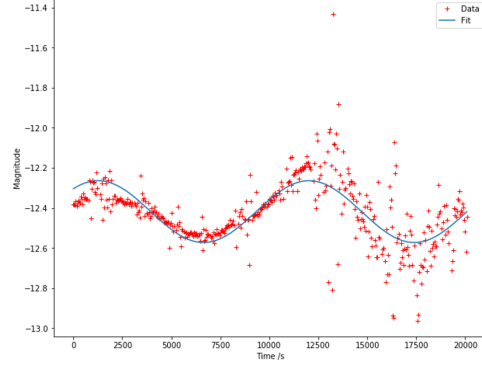
Three different sine wave functions were fitted to the data, as seen in figure 6. Firstly, a single sine wave where the frequency and amplitude were determined by equation 2. Where A_0 is the offset amplitude, A is the amplitude, f is the frequency and ϕ is the phase. The second fit is the result of two sine waves where the amplitudes can vary independently, and the third had varying frequencies and amplitudes. Performing the Fourier transform on the lightcurve produced figure 7. The error on frequency was found from the full width half maximum, FWHM, of the strongest

peak. The analysis of these functions in to determine the rotational period is discussed in the section 3.

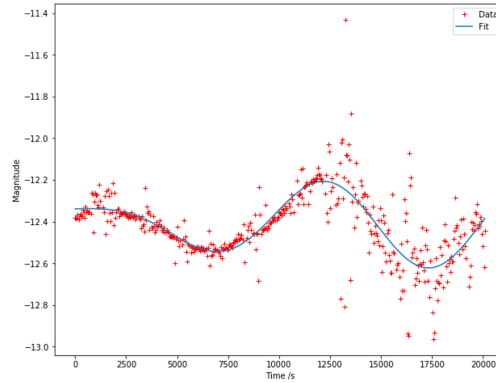
$$y = A_0 + A \sin(2\pi fx - \phi) \quad (2)$$



(a) One sine wave.



(b) Two sine waves where the amplitudes can vary independently.



(c) Two sine waves where the frequency and amplitude can vary independently.

Figure 6: Three models to fit a sine wave to the lightcurve.

2.3 Finding geometric albedo

2.3.1 The "1329 Relation"

Two methods were applied to find the geometric albedo, the first being the application of the "1329 relation", as seen in equation 3. This relates the absolute magnitude, H and the average diameter, D to the albedo, p_v . It was found first so that it could be used to verify the result obtained from the second method which relied on extrapolation, hence being susceptible to larger errors. The diameter was found using the arc length formula. This method is applicable since its angular width is very small, complying to the conditions under which it is valid. The diameter calculated represents the maximum extent across the sky for 694 Ekard, this is because it relies on the maximum arc length measurement.

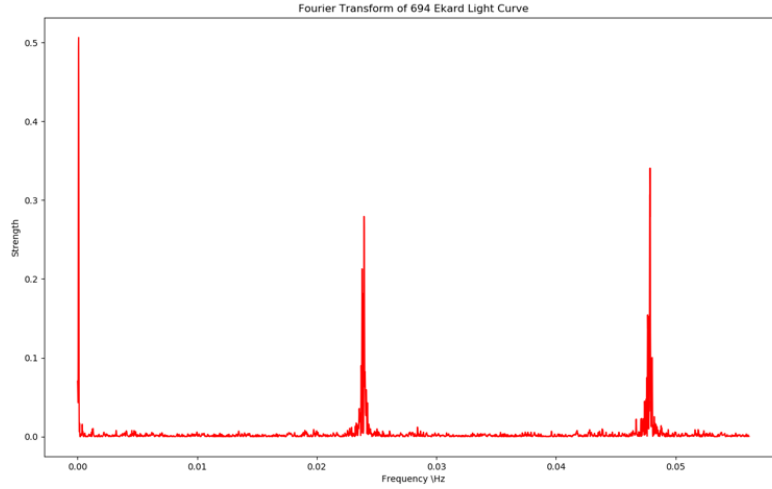


Figure 7: Result of performing a Fourier transform on the Lightcurve from figure 5c. Three dominant frequencies can be seen, as expected. However the two high frequency peaks were not attributed to the components of rotation of the asteroid, as explained in section 3.1.

$$p_v = \left(1329 \times \frac{10^{-\frac{H}{5}}}{D} \right)^2 \quad (3)$$

2.3.2 Phase Model

694 Ekard never actually reaches opposition, the point from which the geometric albedo is defined where the Sun and object form a straight line through Earth. Over a year, it is found to reach a minimum phase angle of 3.1546° , as seen in figure 8. This is not uncommon for asteroids due to the small statistical likelihood of an asteroid lining up exactly with the opposition. As a result, the second method utilises a model to extrapolate the magnitude to the opposition, as suggested by Bowell et al. 1989 [5].

In order to find the albedo, the magnitude as a function of phase angle, α , must be found. First, the visual magnitude, V , has to be normalised to remove variation as a result of changing distances between the object and the Sun and the Earth. This is called the reduced magnitude, $H_v(\alpha)$, and is defined as the magnitude of an object when the object-solar distance, r_h , and the object-observer distance, r_g , both equal 1au, and is given by equation 4. The reduced magnitude as a function of phase angle is modelled by equations 5, 6 and 7.

$$H_v(\alpha) = V(r_h, r_g, \alpha) - 5 \log \left(\frac{r_g r_h}{1 \text{ au} \cdot 1 \text{ au}} \right) \quad (4)$$

$$H_v = H_v(\alpha) + 2.5 \log[(1 - G)\phi_1 + G\phi_2] \quad (5)$$

where ϕ_1 and ϕ_2 are given by

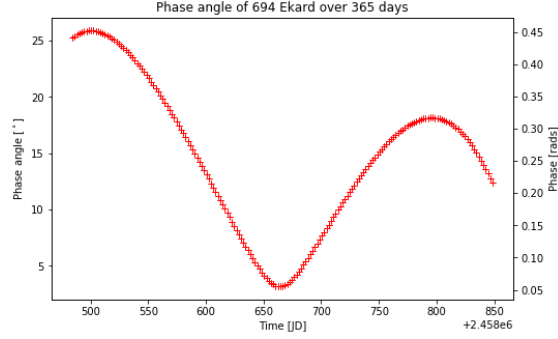


Figure 8: Plotting the phase angle against time from data using from the JPL Horizons module. It can be seen that 694 Ekard never reaches the opposition.

$$\phi_1 = \exp \left[-3.33 \tan^{0.63} \left(\frac{\alpha}{2} \right) \right] \quad (6)$$

$$\phi_2 = \exp \left[-1.87 \tan^{1.22} \left(\frac{\alpha}{2} \right) \right] \quad (7)$$

G is the slope parameter. This describes the non-linear surge in brightness measured when an asteroid approaches the opposition, known as the opposition effect. Two mechanisms have been used to explain this phenomenon. One is the shadow-hiding opposition effect (SHOE) which is where greater proportions of shadowed areas on the walls of craters are hidden at opposition. The other is the coherent back-scattering opposition effect (COBE) where coherent wavefronts of light constructively interfere at opposition [10]. The slope parameter is known for fewer than 0.1% of asteroids, so is given a typical value of 0.15 [11]. This parameter determines the shape of the phase function, and so the magnitude at the opposition can be determined from only one reduced magnitude value and its corresponding phase angle. Since there is available data at multiple phase angles, the opposition magnitude values can be averaged, increasing its reliability. This can then be used as a starting point for the model to estimate the reduced magnitude as a function of the phase angle by rearranging equation 5, making $H_v(\alpha)$ the subject.

Finally, the albedo is found by plotting the irradiance factor, $\frac{I}{F}$, as a function of α . This is defined as the flux per meter squared divided by that of a perfectly diffuse, Lambertian plate of equal projected area. Perfectly diffuse indicates an albedo of unity and Lambertian objects have the same albedo regardless of viewing angle. It is a ratio of the reflected flux and total flux. This is chosen because at opposition, the irradiance factor coincides with the geometric albedo. It is defined by equation 8, where V_\odot is the V-band magnitude of the Sun, $S_{proj}(t)$ is the projected area as a function of time, and $m_c = -5 \log(1AU/1\text{meter})$ is a constant to adjust the length unit.

$$-2.5 \log \left(\frac{I}{F} \right) = H_v(\alpha) - V_\odot - 2.5 \log \left(\frac{\pi}{S_{proj}(t)} \right) + m_c \quad (8)$$

Once the albedo is determined, the asteroid will be classified into a taxonomic class, from which its density and composition can be estimated. The typical albedo and density ranges for each class are stated in table 1.

| Class | Albedo Range | Density Range kg m^{-3} |
|--------|--------------|----------------------------------|
| C-Type | 0.03 – 0.09 | 1570 ± 1380 |
| M-Type | 0.1 – 0.18 | 2000 ± 969 |
| S-Type | 0.1 – 0.22 | 2660 ± 1290 |

Table 1: Table showing the typical albedos and densities for each asteroid taxonomic class[12][13].

Since this classification depends solely on the visible light received, it is only indicative of the surface composition, therefore, it is assumed that the asteroid is homogeneous in terms of composition and density.

3 Results and analysis

3.1 Rotational period

It can be seen from figure 5c that the quality of the data gets worse towards the end of the night, the reason for this was deemed to be poor weather conditions. Figure 6 shows three sine models to fit the data. For the first model, a frequency of $92.952\mu\text{Hz}$ was obtained, the second produced a frequency of $92.9488\mu\text{Hz}$. Despite the third model producing the best fit, it was unable to find a frequency since it was not constant across the data. The second fit produced a period of $2.99 \pm 0.04h$ by applying $T = 1/f$, see appendix 3 for error calculation. This result relies on the frequency from a single sine wave and so assumes the presence of only one component of rotation. This is valid under the condition that the other components have periods are much longer than the observation time and therefore have a negligible effect on the lightcurve within these limits.

To determine the period using a Fourier transform, the strongest peak at $100\mu\text{Hz}$ was analysed. Figure 9 displays a re-scaled image of figure 7, focusing on the highest intensity peak. It can be seen that the peak is not symmetrical and it is believed that this is due to inconsistent seeing effects in the atmosphere; consequently, the errors will also be non-symmetrical. A short program was written to find the peak frequency and the frequencies at FWHM. A peak frequency of $94.6\mu\text{Hz}$ was found with an upper limit frequency of $145\mu\text{Hz}$ and a lower limit frequency of $64.7\mu\text{Hz}$. Giving a period of $2.94_{-0.51}^{+1.36}h$, agreeing with the result from the sine wave fitting method.

The error obtained from the Fourier transform is much larger than that of the result from the sine fitting method. This could be due to the short observation time rendering it difficult for Fourier analysis to obtain a reliable fit for the frequency. A longer observation duration would have reduced the error on the period by increasing the signal strength compared to the noise. Another source of error is inconsistent seeing conditions having the effect of increasing the noise level in the Fourier transform.

The causes of the other peaks at higher frequencies in the Fourier transform were undetermined as they give periods on the order of $\simeq 10s$ which cannot represent a rotational period for this asteroid. Due to the short waveform, it is assumed that this is random noise which would have had a much lower intensity if there were more wavelengths present to be examined by Fourier analysis. The other two components of rotation were assumed to have much larger periods instead, such that their effects do not produce a large enough signal on a lightcurve spanning $5.5h$. Despite this, no compelling peaks were found at frequencies smaller than $50\mu\text{Hz}$.

The retrieved period from both methods was half the value expected from the literature [8].

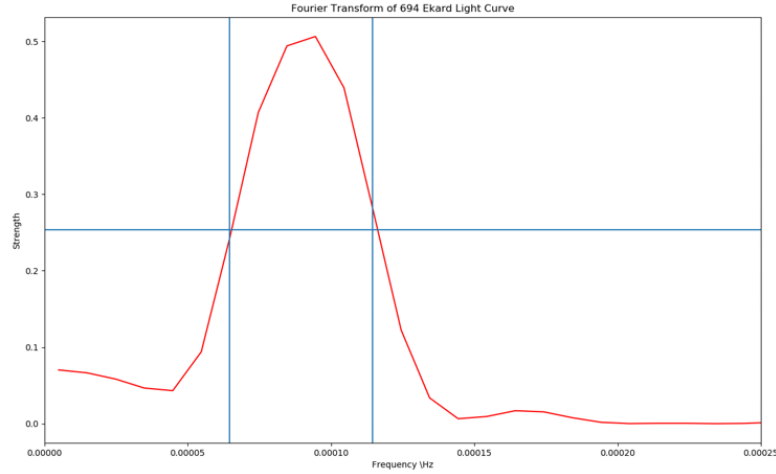


Figure 9: Re-scaling figure 7, focusing on the strongest peak at low frequency. The peak is asymmetric due to errors during observation and short observation time. The blue lines indicate the position of the FWHM to find the upper and lower errors bounds on frequency.

It was determined that aliasing would not have caused this by scaling the result since the period of the asteroid is much larger than the exposure time and hence, the sampling rate, in compliance with Nyquist theorem. In order for the measured period to be half that of the quoted value, it was assumed that one side of the asteroid must be indistinguishable from the other. Indicating that the asteroid has an axis of symmetry along the axis of rotation that produced this signal. This also implies that the surface is homogeneous, otherwise, there would have been distinguishing features on either side of the asteroid, identifying a period from a half period. Perhaps the degrading quality of the lightcurve towards the end of the observation contributed to this by shrouding small variations in the lightcurve.

Nevertheless, the periods were multiplied by two, obtaining $5.98 \pm 0.08h$ from the sine fitting method and $5.87^{+2.71}_{-1.02}h$ from the Fourier transform method, agreeing with the literature [8].

3.2 Shape and Geometric albedo

3.2.1 Determining the Shape

In order to find the geometric albedo, the area of the reflecting surface as a function of time must be found first. In anticipation of this, the diameter was found using the arc length approximation. A Plot diameter against time can be seen in figure 10, giving a mean diameter of 121.891 ± 3.657 km, agreeing with the results stated by the JPL Small-Body Database Browser. By approximating the reflecting area as a circular disk, as per the Lambertian plate assumption. This gives an average projecting area of 11668 ± 0.30 km², see appendix 4 for error calculation.

Assuming that Ekard resembles a tri-axial ellipsoid, the extents in each axis can be determined using the relations in appendix 5. This assumption is based on the prediction of the presence of an axis of symmetry from section 3.1. Each extent is labelled by decreasing size as a, b and c, where c is along the axis of rotation [14]. These were found to be $a = 138.026 \pm 4.141$ km,

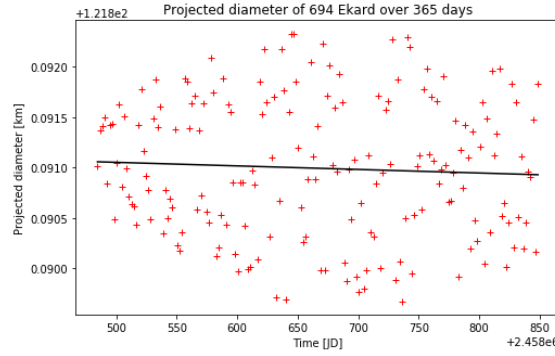


Figure 10: Diameter measurements as a function of time. These were found using the arc length approximation where the angle subtended is given by the maximum angular extent. This results in a mean diameter measurement of 121.891km.

$b = 125.478 \pm 3.764$ km and $c = 104.565 \pm 3.137$ km. From these, its shape can be plotted by using the ellipsoid equation. This gives the shape in figure 11 and a volume estimate of $(2.414 \pm 0.125) \times 10^6$ km³.

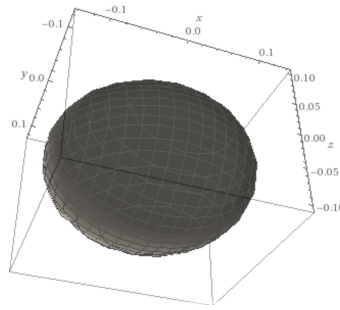


Figure 11: Modelling the shape of 694 Ekard from the tri-axial extents, a , b , c . Note that the axis has been scaled by a factor of 0.001.

3.2.2 Geometric Albedo

To find the albedo from the 1329 method, the magnitude was quoted from the JPL Small-Body Database alongside the calculated average diameter to get an independent value of albedo of 0.026 ± 0.004 for the asteroid. This would be used to verify the result from the phase model.

In order to apply the phase model, first a starting point for the function needed to be defined. This was done by extrapolating all reduced magnitude measurements to the opposition, giving an average reduced magnitude at the opposition of 9.201 ± 1.022 , where the error is found from the standard deviation of results. The evolution of the reduced magnitude as a function of α was plotted using the phase function and was overlaid with the raw data points, as seen in figure 12. The agreement between observation and what the model predicts suggests a good model.

Using equation 8, the irradiance factor can be found as a function of alpha as shown in figure 13, where α is an evenly spaced set of numbers between zero and 25.9° , the maximum phase

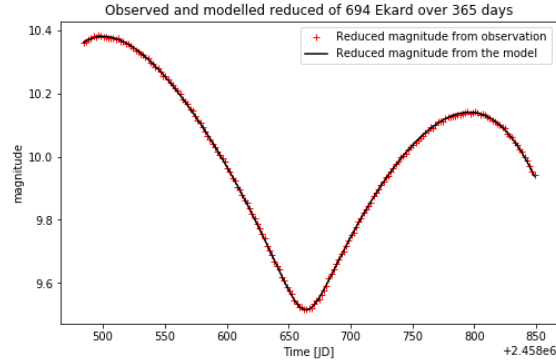


Figure 12: The reduced magnitude of 694 Ekard as a function of time. The crosses are results from observations and the black line is the prediction from the model. The agreement between them suggests accuracy in the model.

angle reached by 694 Ekard. It can be seen that there are no red crosses at phase angles less than 3.1546° , affirming the fact 694 Ekard never reaches opposition.

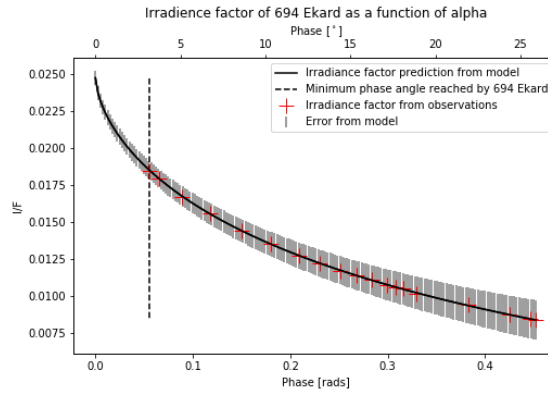


Figure 13: The irradiance factor as a function of the phase angle. The vertical dotted line indicates the position of the minimum phase angle reached by 694 Ekard, and it can be seen that there are no red crosses at angles smaller than this.

The value of the irradiance factor at opposition provides the geometric albedo as 0.025 ± 0.001 , agreeing with the prediction from the 1329 relationship. This classifies 694 Ekard as a C-type asteroid, therefore it can be expected to have a density of $1570 \pm 1380 \text{ kg m}^{-3}$. Along with the volume estimate, this gives a mass estimate for 694 Ekard of $(3.791 \pm 3.338) \times 10^9 \text{ kg}$, see appendix 8 for error calculation. Due to the nature of the model, extrapolation further from opposition incurs greater errors. Other errors may arise from imperfect phase function modelling or weather effects present in the Horizons database.

It has been suggested that asteroids may have a lower albedo as a function of the orbital radius, especially if they have smaller inclination angles [15]. This is due to them becoming covered in a layer of dust from the galactic plane. By plotting the albedo of asteroids as a function of average orbital radius, a straight line equation can be obtained, as seen in figure 14. This can be used

to correct the albedo of 694 Ekard to account for the dust. This suggests that 694 Ekard could have an albedo as high as 0.20, classifying it as an S-Type asteroid, ergo implying a much larger proportion of metal and approximately double the density. However, this deduction is highly subjective to observational biases and therefore should be treated with scepticism.

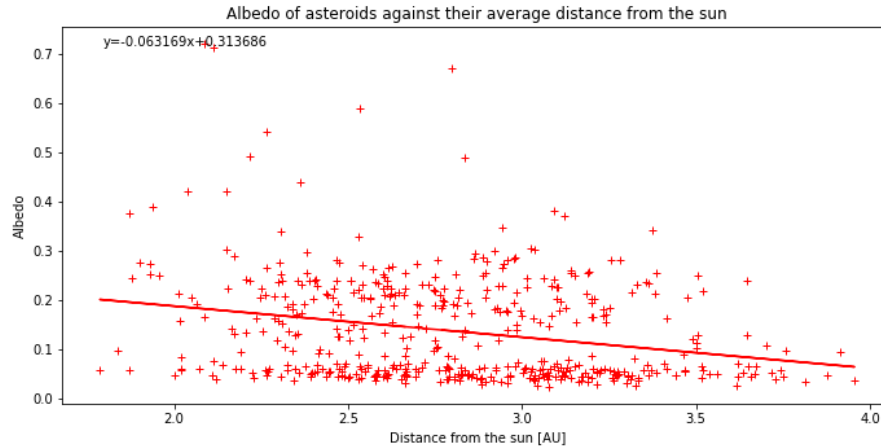


Figure 14: The albedo as a function of the average orbital radius for 500 asteroids. This plot is subject to change as the number of asteroid discoveries increases.

4 Conclusion and Further Areas of Research

This lab project set out to determine the properties of 694 Ekard and discern whether it is a suitable candidate for mining. The criteria for asteroid selection and the reduction plan was made with regard to three asteroids we planned to view from Birmingham, 18172 (2000 QL7), 162723 (2000 VM) and 99248 (2001 KY66) but was instead applied to 694 Ekard due to poor weather conditions. 694 Ekard was found to have a rotational period of $5.87^{+2.71}_{-1.02}h$, one standard deviation from values quoted in literature, a diameter of 121.891 ± 3.657 km, agreeing with the literature to 3 d.p, a volume of $(2.414 \pm 0.125) \times 10^6$ km³, an albedo of 0.026 ± 0.001 , agreeing with values quoted in literature [8], and a mass of 3.791 ± 3.338 kg.

Based on these values, 694 Ekard has a rotational period shorter than average [7] and is larger and heavier than average [16][17]. These values alone give the impression that 694 Ekard may be feasible for profitable metal-ore mining. However, due to its taxonomic class, it is unlikely to have a large metal content. Consequently, until space missions become much cheaper to execute, miners would struggle to turn a profit from mining 694 Ekard. However, it has been suggested that C-type asteroids contain an abundance of carbon, ingredients necessary for fertilisers and water [18] which, although may not be as valuable on Earth, are highly useful for space missions by providing nutrients.

A large source of error when calculating the rotational period originated from the observation being shorter than the period of 694 Ekard resulting in difficulty in producing a reliable frequency spectrum. Future investigations may want to observe 694 Ekard on multiple nights to stitch together lightcurves to have a longer function to analyse. This would reduce the noise that was prominent in our Fourier transform. In this case.

When classifying the 694 Ekard, a few crude assumptions were made. The albedo was used to place the asteroid into a taxonomic class based on fairly broad definitions. This is because that research into the taxonomy of asteroids is in its early stages and that probing the inner composition of asteroids still presents challenges. It is expressed by the large error present on the mass estimation of 694 Ekard. It also translates into the inability to define the specific composition of 694 Ekard by proportions of its elements; rather, all that can be said is that it is mainly composed of rock and clay. A more accurate measure of the surface composition could be made using spectral analysis. Also, the mass of the asteroid could be determined more accurately using the dynamical method, whereby measuring gravitational perturbations as the result of interactions between the target body and another [19]. The shape of 694 Ekard presented in figure 11 assumes it is an ellipsoid, this can be more accurately determined using the lightcurve inversion technique [20]. These methods were outside the scope of this paper.

5 Acknowledgements

I would like to give thanks to Sean McGee for running the lab module and sacrificing his time to obtain observational data for all the groups. Also thanks to the demonstrators, Oliver Hall, Emma Willett and Cressida Cleland for helping us with our questions throughout the term. I would like to thank Yoonsoo P. Bach for taking the time to help me understand the Irradiance model used in his paper. Finally, I would like to thank my lab partners Maciej Dabrownny, Astle Fernandez and Ciaran Garden for their contributions for the project.

References

- [1] R. Gomes, H. F. Levison, K. Tsiganis, and A. Morbidelli, “Origin of the cataclysmic late heavy bombardment period of the terrestrial planets.”
- [2] I. Belskaya and C.-I. Lagerkvist, “Physical properties of m class asteroids,” Feb 1999.
- [3] L. Glaze, “In depth.”
- [4] J. Fowler and J. Chillemi, “Iras asteroid data processing,” *The IRAS Minor Planet Survey*, vol. 17, 1992.
- [5] E. Bowell, B. Hapke, D. Domingue, K. Lumme, J. Peltoniemi, and A. W. Harris, “Application of photometric models to asteroids,” in *Asteroids II*, pp. 524–556, 1989.
- [6] “Exposure time calculations.”
- [7] C.-I. Lagerkvist, M. Dahlgren, A. Ekholm, J. Lagerros, M. Lundström, P. Magnusson, *et al.*, “10. colours of distant solar system bodies,” in *Proceedings of the ESO Workshop Held at Garching*, vol. 2, p. 5, Springer, 1998.
- [8] “Jpl small-body database browser.”
- [9] P. Sorensen, “Object visibility – staralt,” 2002.
- [10] M. Lee and M. Ishiguro, “Opposition effect on s-type asteroid (25143) itokawa,” *Astronomy & Astrophysics*, vol. 616, p. A178, 2018.

- [11] K. Muinonen, I. N. Belskaya, A. Cellino, M. Delbò, A.-C. Levasseur-Regourd, A. Penttilä, and E. F. Tedesco, “A three-parameter magnitude phase function for asteroids,” *Icarus*, vol. 209, no. 2, pp. 542–555, 2010.
- [12] D. R. Williams, “Asteroids,” Nov 2018.
- [13] G. A. Krasinsky, E. V. Pitjeva, M. V. Vasilyev, and E. Yagudina, “Hidden mass in the asteroid belt,” *Icarus*, vol. 158, no. 1, pp. 98–105, 2002.
- [14] J. D. Drummond, A. Conrad, W. Merline, B. Carry, C. Chapman, H. Weaver, P. Tamblyn, J. Christou, and C. Dumas, “The triaxial ellipsoid dimensions, rotational pole, and bulk density of esa rosetta target asteroid (21) lutetia,” *arXiv preprint arXiv:1005.5353*, 2010.
- [15] A. Kazantsev, “Spatial separation effect of asteroids with different albedos,” *arXiv preprint arXiv:0806.2717*, 2008.
- [16] E. L. Ryan, D. R. Mizuno, S. S. Shenoy, C. E. Woodward, S. Carey, A. Noriega-Crespo, K. E. Kraemer, and S. D. Price, “The kilometer-sized main belt asteroid population revealed by spitzer,” *Astronomy & Astrophysics*, vol. 578, p. A42, 2015.
- [17] B. Carry, “Density of asteroids,” *Planetary and Space Science*, vol. 73, no. 1, pp. 98–118, 2012.
- [18] M. J. Sonter, “The technical and economic feasibility of mining the near-earth asteroids,” *Acta Astronautica*, vol. 41, no. 4-10, pp. 637–647, 1997.
- [19] O. Kochetova, “Determination of large asteroid masses by the dynamical method,” *Solar System Research*, vol. 38, no. 1, pp. 66–75, 2004.
- [20] J. Ďurech, M. Kaasalainen, D. Herald, D. Dunham, B. Timerson, J. Hanuš, E. Frappa, J. Talbot, T. Hayamizu, B. D. Warner, *et al.*, “Combining asteroid models derived by lightcurve inversion with asteroidal occultation silhouettes,” *Icarus*, vol. 214, no. 2, pp. 652–670, 2011.

6 Appendix

1. In this instance, an orbit would rarely be a gravitational orbit due to asteroids generally having small masses, rather it would be one forced by jets or with a tether.

2. To calculate the integration time, bright conditions were assumed to obtain a worst case scenario. The telescope specifications state that under these conditions, 7.6×10^4 photons are collected from a 16.7mag source in 10 minutes and with an SNR of 10. First the number of photons collected from our 16.5mag source needed which is calculated using the magnitude equation.

$$m_1 - m_2 = -2.5 \log \left(\frac{f_1}{f_2} \right).$$

Where m_i is the magnitude of an object or the sky and f_i is its corresponding flux.

$$f_2 = 7.6 \times 10^4 \times 10^{\left(\frac{16.7-16.5}{2.5}\right)} = 1.2f_1 = f_{obj}.$$

$$t = SNR^2 \frac{f_{obj} + f_{sky}}{f_{obj}^2}.$$

$$t = 10^2 \frac{1.2 \times 7.6 \times 10^4 + 7.6 \times 10^4}{1.2 \times 7.6 \times 10^4} \times 600 = 28.9 min.$$

3. Error on period calculation where T is the rotational period and f is the frequency.

$$\delta T = \sqrt{\frac{1}{f^2}} \delta f.$$

4 Error calculation for projected area. The JPL Horizons database stated that results of distance between the object and the sun or the observer were subject to a 3% error.

$$\delta S_{proj} = 2S_{proj} \frac{\delta r_g}{r_g}.$$

5. Determining the tri-axial extents where $\mu = \frac{a}{b} = 1.2$ and $\nu = \frac{b}{c} = 1.1$ [14].

$$a = d(\mu^2 \nu)^{\frac{1}{3}}. \quad b = d\left(\frac{\nu}{\mu}\right)^{\frac{1}{3}}. \quad c = \frac{d}{(\mu \nu^3)^{\frac{1}{3}}}.$$

6 Error on the albedo from the "1329 relation" is given by the following formula, where p_v is the geometric albedo. δV is the error on the visual magnitude and is quoted on the JPL Horizons database to have a typical value of ± 1 .

$$\delta p_v = 2p_v^{\frac{3}{2}} \sqrt{\left(\frac{\delta D}{D}\right)^2 + \left(\frac{\ln 10}{5} \delta V\right)^2}.$$

7 Error on irradiance formula, where H_0 Is the reduced magnitude at opposition.

$$\delta\left(\frac{I}{F}\right) = 10^{\frac{2}{5}(H-V_{\odot}+m_c)} \left[\left(\delta H_0 \frac{2 \ln(10)}{5} 10^{-\frac{2}{5} \log(\frac{\pi}{S_{proj}})} \right)^2 + \left(\frac{\delta S_{proj}}{S_{proj}} 10^{-\log(\frac{\pi}{S_{proj}})} \right)^2 \right]^{\frac{1}{2}}.$$

8 Error calculation for mass. This was subject to a large error due to the large uncertainties associated with the density of C-type asteroids, where M is the mass of the asteroid, and ρ is its density.

$$\delta M = \sqrt{\left(\frac{\delta V}{V}\right)^2 + \left(\frac{\delta \rho}{\rho}\right)^2}.$$